Electronic and lattice instability and its relaxation mechanism in Pt-Co interfaces

Wai-Leung Yim[1,*] and Thorsten Klüner[2]

[1]*Institute of High Performance Computing, 1 Fusionopolis Way, #16-16 Connexis, Singapore 138632*

[2]*Institut für Reine und Angewandte Chemie, Theoretische Chemie, Carl von Ossietzky Universität Oldenburg, D-26129 Oldenburg, Germany*

(Received 30 December 2010; revised manuscript received 9 January 2012; published 23 January 2012)

Lattice instabilities of bimetallic Pt-Co interfaces have been examined within density functional theory. We discovered that the lattice instability and electron instability in momentum space were strongly correlated on bimetallic interfaces. The lattice instability of the Pt-Co interface was illustrated by Fermi surface nesting in two dimensions, and the nesting vector along the (110) direction in electron momentum space has been identified. The predicted reconstruction-induced Pt diffusion trend was in excellent agreement with previously obtained experimental findings.

DOI: 10.1103/PhysRevB.85.035435 PACS number(s): 68.35.Ja, 61.66.Dk, 63.22.Np, 63.20.dk

I. INTRODUCTION

Bimetallic Pt-Co systems have many practical applications, e.g., as a catalyst or magnetic storage material.[1,2] The chemical properties of Pt-Co systems strongly depend on the surface composition.[3–5] However, the formation dynamics of this interface and the underlying physical mechanism are still unknown. There was some indirect experimental evidence of atomic diffusion of Pt and Co as a function of preparation temperature. Low-energy electron diffraction (LEED) experiments showed that the segregation tendency depended on the thickness of the cobalt overlayer—the segregation started at 200 and 400 °C for a 2–3-ML and a 6-ML cobalt overlayer, respectively. The equilibrium structures were obtained by annealing the samples at 400 °C.[6,7] It is extremely important to understand the initial Pt diffusion step in atomic detail, which will facilitate the design of bimetallic compounds of higher thermal stability. For example, very recent experimental findings by Cao and Veser *et al.* revealed new fundamental insight into thermal stability, which is important for particles of practical use.[8] By carefully controlling composition, PtRh nanoparticles were thermally stable even at 830 °C. Some PtRh particles exhibited (100)-like outer surfaces.[8] The relationship between this unexpectedly high thermal stability and surface morphology is still not clear.

We studied the lattice instability of the Co/Pt(111) interface, its softening mechanism, and its consequence on intermetallic mixing by density functional theory (DFT). The Co overlayers of different thickness were found to be unstable. For Co overlayers $\geqslant$3 ML, the overlayers were transformed from Co(111) to Co(100) spontaneously. The Co(100) overlayers were resistant to thermal deformation. The origin of transformation from (111) to (100) overlayer was due to the electron instability in **k** space by Fermi surface nesting. As a consequence, the Co(100)/Pt(111) interface was formed and the outer surface was stabilized when the Co overlayer was sufficiently thick. The Pt diffusion barriers were affected by the orientation and thickness of the Co overlayer. Overall, we suggest that the higher thermal stability of Pt-Co surfaces with thicker Co overlayers can be traced back to the heteroepitaxial reconstruction of cobalt overlayer.[6,7]

II. COMPUTATIONAL DETAILS

We have made use of PWscf and Vienna Ab Initio Simulation Package (VASP) because of their merits with regard to linear-response theory and the high efficiency of molecular-dynamics (MD) simulations, respectively.[9–12] Using PWscf, surface structures were optimized and their phonon structures were calculated by density functional perturbation theory (DFPT).[12,13] Slab models in (1 × 1) supercells were used to simulate the alloy surfaces. For Co(111)/Pt(111) systems, the interfacial cobalt atoms were located in the fcc hollow sites of the Pt(111) interfaces.[14] Co/Pt(111) slabs with different thickness of cobalt overlayers (1–4 ML) on a 6-ML Pt(111) substrate were considered. The separation between next-neighboring slabs was set to 13 Å to avoid spurious interactions. Computational parameters are summarized in Table I.

III. RESULTS AND DISCUSSIONS

In the Perdew-Burke-Ernzerhof functional with ultrasoft pseudopotential (PBE-USPP) calculations by PWscf, the optimized lattice constants of bulk Pt (fcc) and Co (hcp) were found to be 3.998 and 2.491 Å, respectively, which are in very good agreement with the experimental values of 3.924 and 2.507 Å, respectively.[21,22] We have calculated the phonon band structures of the bare Pt(111) slab of 3 ML, and the bare Co(111) slabs of 3, 4, and 5 ML, using their corresponding crystal lattice constants. These bare surfaces were found to be stable by *ab initio* phonon calculations. On the Pt(111) substrates, the Co(111) overlayers exhibited considerable magnetic moments as shown by the Perdew-Burke-Ernzerhof functional with projector augmented wave (PBE-PAW) approach implemented in VASP. For instance, on a 9-ML Pt(111) surface slab, one Co monolayer exhibited a magnetic moment of 2.5 μ_B/atom, while the thicker Co overlayers in (111) orientation had their magnetic moments ranging from 1.91 μ_B/atom [6-ML Co(111)] to 2.06 μ_B/atom (2-ML Co). Here, the magnetic moment was the averaged moment within the cobalt overlayer.

The phonon density of states (PDOS) of the 1–4 ML Co(111) overlayers on the 6-ML Pt(111) slabs is displayed in Fig. 1(a). The Co monolayer and bilayer adsorbed on the 6-ML Pt(111) were unstable [cf. Figs. 1(a) and 1(b)]. We will show later that these two structures virtually maintain their Co(111) form in molecular-dynamics simulations. Beyond a coverage of 2-ML Co, the 3- and 4-ML cobalt overlayers also exhibit a soft acoustic branch [cf. Figs. 1(c) and 1(d)]. Interestingly, the thickness-dependent orientational

TABLE I. Computational parameters in DFT calculations.

	PBE-USPP[15,16]	PBE-PAW[15,17]
software	PWscf	VASP
pseudopotential	Ultrasoft	PAW
Ψ_{cutoff} (Ry)[a]	50	20[d]/15[e]
ρ_{cutoff} (Ry)[b]	400	35
smearing	Marzari-Vanderbilt[18]	Methfessel-Paxton[19]
σ (Ry)[c]	0.015	0.015
k mesh[20]	$6\times6\times1$[f]/$8\times8\times1$[g]	$6\times6\times1$[d]/$3\times3\times1$[e]
q mesh[13]	$3\times3\times1$[f]/$4\times4\times1$[g]	

[a] Ψ_{cutoff} is the plane-wave energy cutoff.
[b] ρ_{cutoff} is the charge-density energy cutoff.
[c] σ is the width of the Gaussian smearing.
[d] For geometry optimization and single point calculations.
[e] For MD simulations.
[f] For 3-, 4-, and 5-ML Co overlayers.
[g] For 1- and 2-ML Co overlayers.

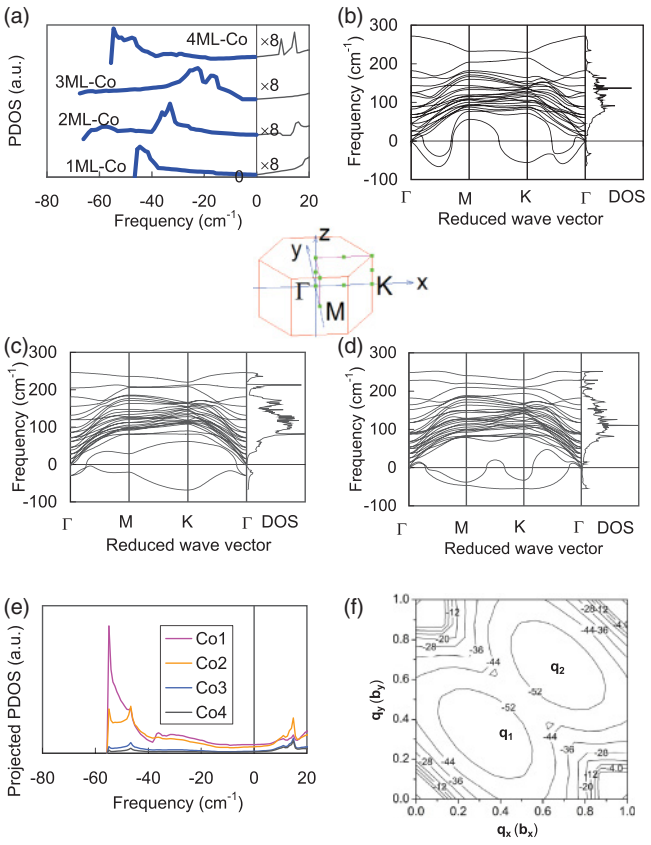

FIG. 1. (Color online) (a) Phonon density of states of 1–4-ML Co(111) on 6-ML Pt(111) substrates. The negative (imaginary) frequency parts are marked in blue. (b) Phonon dispersion relation of 2-ML Co/6-ML Pt(111). The first Brillouin zone of a hexagonal lattice is shown. (c) Phonon dispersion relation of 3-ML Co(111)/6-ML Pt(111). (d) Phonon dispersion relation of 4-ML Co(111)/6-ML Pt(111). (e) Projected PDOS of 4-ML Co(111)/6-ML Pt(111). The outermost cobalt layer was labeled as Co_1. (f) Contour of the vibrational frequency of the softest mode along the $\mathbf{q}_x$-$\mathbf{q}_y$ plane in 4-ML Co(111)/6-ML Pt(111). $\mathbf{b}_x$ and $\mathbf{b}_y$ were the basis vectors of the reciprocal lattice.

preference was not only found in the Pt-Co system, but was also observed experimentally in other systems such as ZnO(0001)/Ag(111).[23] Figure 1(e) shows that the soft phonon band is entirely due to the soft vibrational motions of the cobalt overlayers, particularly at the topmost cobalt monolayer. The softest vibrational mode can be located by drawing a contour plot of the softest vibrational frequency in the first Brillouin zone [cf. Fig. 1(f)]. The two softest $\mathbf{q}$ vectors were located, namely $\mathbf{q}_1$ (0.4,0.4,0.0) and $\mathbf{q}_2$ (−0.4,−0.4,0.0) [Fig. 1(f)]. The soft acoustic mode near the zone boundary indicated that the structure in the (1×1) supercell is not stable, and the size of the supercell was finally doubled in order to relieve the lattice instability.

The Fermi surface nesting rationalizes the direction of relaxation. Figure 2(a) displays the Fermi contour of α electrons (majority spin) in the 4-ML Co(111)/6-ML Pt(111) slab. The β electron (minority spin) also displays a similar pattern. The flat bands of the Fermi surface can clearly be seen. One of the electronic bands exhibited a sharply elongated hexagonal Fermi contour [cf. Fig. 2(b)]. The two parallel Fermi contours were coupled with two nesting vectors, $\mathbf{q}_1$ and $\mathbf{q}_2$, which explains the two lobes of the phonon softening pattern in Fig. 1(f). The flat electronic band from $\mathbf{P}_1$ to $\mathbf{P}_2$ [labeled in Fig. 2(b)] is shown in Fig. 2(c). Both α and β electronic bands contain a large amount of the flat band dispersion near the Fermi level, which is the origin of the electronic instability. In particular, the β electronic band lies almost exactly at the Fermi level. The eigenvectors of the topmost Co layer corresponding to the soft mode at $\mathbf{q}=(0.5,0.5)$ are displayed in Fig. 2(d). The high symmetry of the (111) face is distorted so that the cobalt atoms tend to form dimers within the intralayer. The atomic motions along the soft mode lead to the structural relaxation and form an energetically more stable phase.

Lattice-dynamics analysis is a first-order analysis. The energy of the system can be expanded by Taylor series. Generally, the DFT program packages take the first three terms into account, i.e., $V(R_0)$, $\nabla E(R_0)$, and $\nabla^2 E(R_0)$, where $V(R_0)$ is the energy at equilibrium R_0, $\nabla E(R_0)$ is the energy gradient with respect to atomic displacement, and $\nabla^2 E(R_0)$ is the second derivative of energy with respect to atomic displacements of two atoms ($\partial^2 E/\partial q_1 \partial q_2$). For the periodic system, one may suppress the lattice instability simply by selecting an incommensurate supercell. In this Pt-Co system, the stable structure is of incommensurate phase. So, although the DFT program package optimizes the structure to the energy minimum, this structure may be at the saddle point with respect to the lattice degree of freedom. By *ab initio* phonon calculations, the lattice instability can be identified. A positive-definite Hessian matrix guarantees a stable structure according to the harmonic approximation. However, when the structure is largely distorted, i.e., beyond the quadratic approximation, some higher-order terms have to be considered in order to predict the final structures. In other words, the soft vibrational mode indicates the initial deformation mechanism only. A stable structure can be achieved by thermally annealing. Therefore, the geometry of the stable structure will be accessible in the end of the trajectory.

The lattice stability of the cobalt overlayers was verified by *ab initio* MD simulations using the PBE-PAW method. The slab models contained 1–4 ML of cobalt, which was

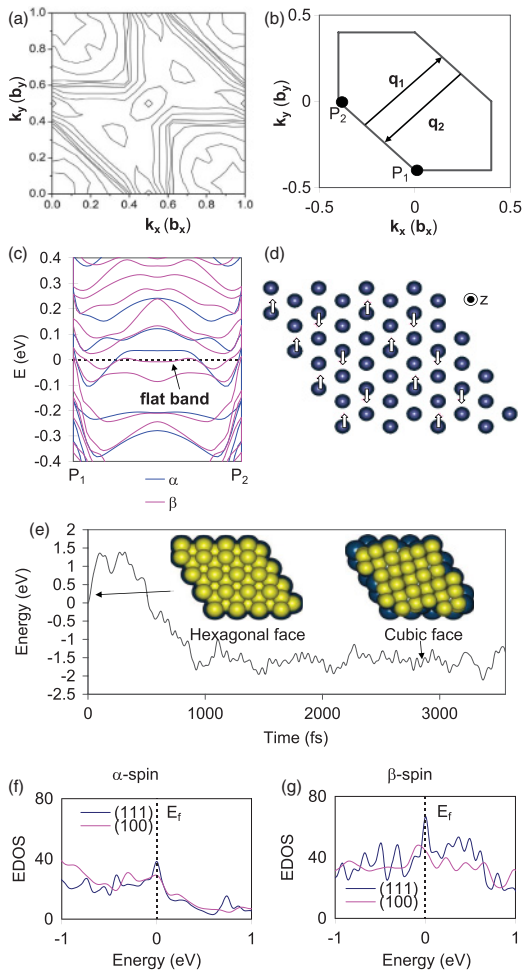

FIG. 2. (Color online) (a) Fermi contour of 4-ML Co(111)/6-ML Pt(111) in a (1×1) supercell. (b) Schematic diagram of the Fermi contour after shifting the origin. The Fermi surface nesting vectors are labeled $\mathbf{q}_1$ and $\mathbf{q}_2$. In (a) and (b), Fermi contours of α spin are shown. (c) Electronic band structure along $\mathbf{P}_1$ and $\mathbf{P}_2$ as labeled in (b). Both α spin (blue) and β spin (red) are shown. (d) The soft mode corresponding to $\mathbf{q} = (0.5,0.5)$ is shown. The arrows illustrate the atomic displacement of the topmost Co layer. (e) Profile of structural transformation of 4-ML Co(111)/6-ML Pt(111) from (111) to (100) faces at 300 K. Pt and Co atoms are shown by blue and yellow, respectively. (f) Electronic density of states of α electrons for Co(111) and Co(100) overlayers. (g) Electronic density of states of β electrons for Co(111) and Co(100) overlayers. In (f) and (g), the unit of EDOS is in states/eV/cell, and the energy is relative to the Fermi energy.

deposited on a 6-ML Pt(111) substrate. The composite slab was located in a (2 × 2) supercell and the next-neighboring images were separated by 13 Å. The optimized structure by PBE-USPP was taken as the starting geometry of the *ab initio* MD calculation. The three bottommost Pt layers were fixed in their optimized positions, while all other atoms were allowed to move. We started the MD simulations with the hexagonal (111) orientation of cobalt. For the model slabs consisting of 1–2 ML of cobalt, this orientation was virtually retained after 5-ps simulations equilibrating at 300 K using a Nosé thermostat.[24] On the other hand, both 3- and 4-ML cobalt overlayers were transformed from Co(111) to Co(100) [cf. Fig. 2(e)]. In these cases, the lateral expansion from Co(111) to Co(100) relieved the lattice mismatch between the cobalt overlayers and the Pt(111) substrate, which was corroborated by a compression normal to the surface. The electronic density of states was obtained for both Co(111) and Co(100) faces of α [Fig. 2(f)] and β spins [Fig. 2(g)], respectively. In Co(111), we can see that both the α- and β-spin electrons showed Fermi instability, i.e., a sharp EDOS peak at the Fermi level. Such a Fermi instability can be significantly reduced by structural relaxation to the Co(100) face.

Figure 3 illustrates the intralayer Co contribution to the projected electronic density of states. In the Co(111) orientation, both α and β spins exhibited a Fermi instability at the Fermi level. In particular, the instability was mainly due to the interfacial cobalt atoms. This can be observed in Fig. 3(a), where the fourth layer (i.e., the interfacial cobalt) has the highest PDOS at the Fermi level among all the cobalt overlayers. Figure 3(b) shows a larger contribution by the third and fourth cobalt overlayers at β spin. After the cobalt reconstructed, the PDOS of the third and fourth cobalt layers changed remarkably. So, the layer-by-layer analysis revealed that the driving force of reconstruction was predominately due to the interfacial cobalt layers.

The instability of the 1-ML cobalt overlayer was not obvious in the MD calculations. On a time average, the cobalt atoms were located apparently at the fcc hollow sites. However, the real-time simulation showed that the cobalt atoms tended to pair up as observed in the MD trajectory. To illustrate this, we computed the radial distribution functions (RDF's) of intralayer Pt-Pt (topmost Pt layer) and intralayer Co-Co separations. The RDF is defined as

$$\mathrm{RDF}(r') = \sum_t \sum_{i \neq j} \delta[|r_i(t) - r_j(t)| - r'].$$

We can use the intralayer RDF as the reference, since the Pt atoms were moving around their equilibrium fcc sites. As shown in Fig. 4(a), we plotted the RDF from 0 to 5.45 Å. Two sharp RDF peaks of intralayer Pt-Pt existed, which revealed that the Pt atoms were confined in their fcc sites. The RDF of Co-Co, however, showed three peaks: the central peak appeared at the same position as the Pt-Pt peaks, and there were two satellite peaks for the first next neighbor. The satellite peaks were attributed to the dimerization of two Co atoms. Figures 4(b) and 4(c) illustrate the dimerization of Co-Co at the 1000th and 2000th time steps, respectively.

We have also performed MD calculations at 300 K, starting from the 1–2 ML of cobalt in the Co(100) orientation. Interestingly, the cobalt monolayer recovered the Co(111) structure while the 2-ML Co film retained a (100) orientation. Ultimately, we observed that (i) the cobalt monolayer exhibits (111) orientation only; (ii) the 2-ML Co film exhibits both orientations; and (iii) the 3- and 4-ML cobalt films exhibit (100) orientation only. To understand the structural preference of the different overlayers, PBE-PAW calculations were performed to optimize the structures of the cobalt overlayers supported by the 6-ML Pt(111) substrate (cf. Fig. 5). We found that the Co(100) structures were more stable than the Co(111) orientation for thicker cobalt overlayers ($\geqslant$2 ML). For the 2-ML Co film, the (100) orientation was lower in energy by

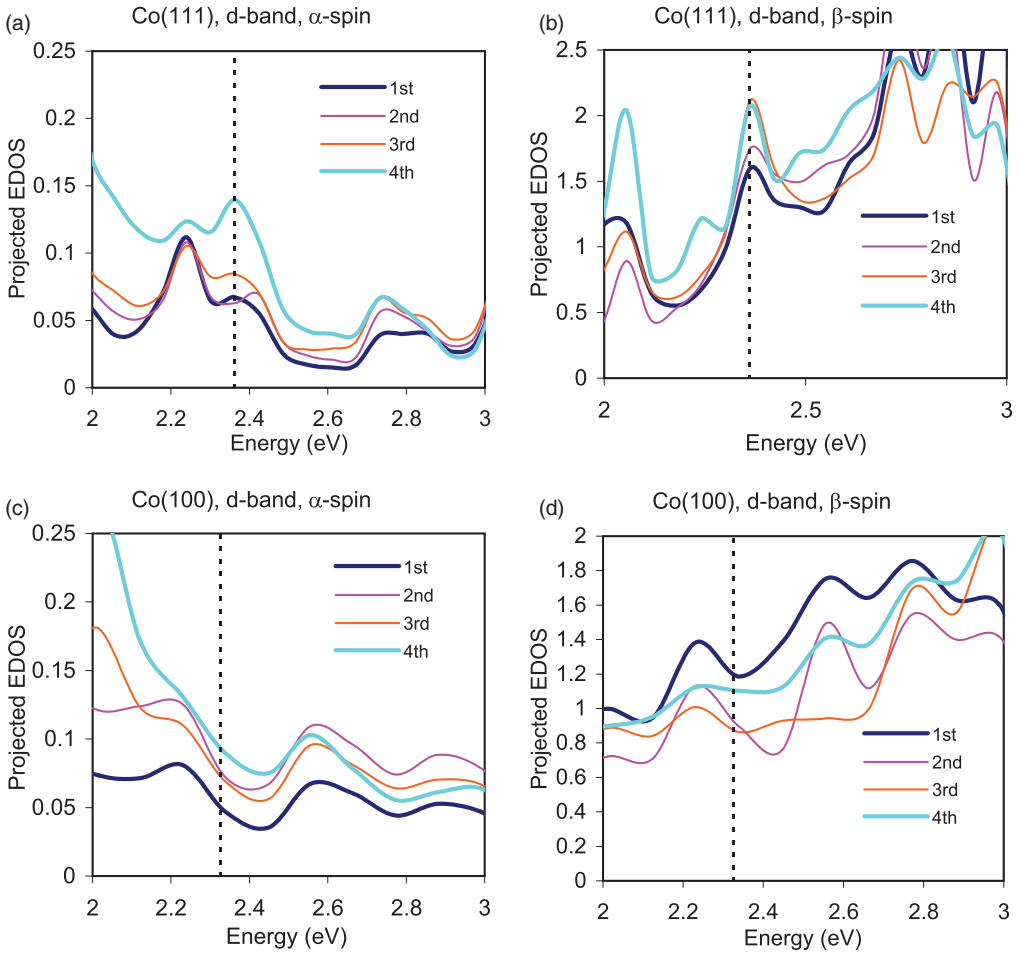

FIG. 3. (Color online) Projected electronic density of states (EDOS) of the first (or topmost, blue), second (red), third (orange), and fourth (cyan) layer of the 4-ML Co/6-ML Pt(111) sample. (a) α spin of Co(111). (b) β spin of Co(111). (c) α spin of Co(100). (d) β spin of Co(100). In (a)–(d), the Fermi energies are represented by dotted lines.

0.27 eV as compared to the Co(111) surface. A considerable transition barrier could be expected, since the two phases were distinguishable in our MD calculations. For thicker cobalt overlayers, the (100) orientation is more stable than the (111) orientation, where the energy differences between the two orientations are 1.13 and 2.10 eV for the 3- and 4-ML cobalt overlayers, respectively. The large energy difference was the reason for the exclusive occurrence of the rectangular phase for these surface slabs. It should be mentioned that the structural transition was also corroborated by a change in the magnetic structure. The larger the reduction of the magnetic moment was, the larger the energy difference between the hexagonal and the rectangular phases turned out to be.

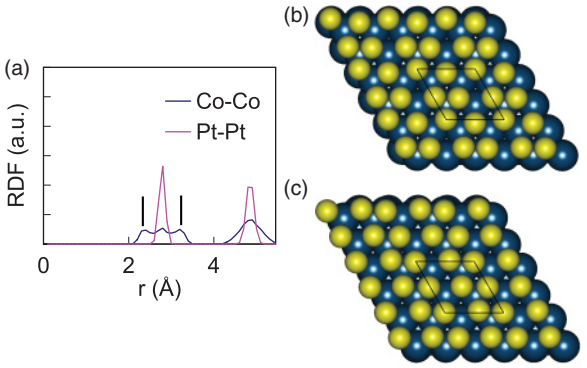

FIG. 4. (Color online) (a) Intralayer radial distribution function of Pt-Pt (topmost, red) and Co-Co (blue) in 1-ML Co(111)/6-ML Pt(111) in a (2×2) supercell. (b) Snapshot of the 1-ML Co(111)/6-ML Pt(111) at the 1000th time step. (c) Snapshot of the 1-ML Co(111)/6-ML Pt(111) at the 2000th time step. The periodic unit cell was labeled in a parallelogram in (b) and (c).

Furthermore, the segregation pathways were elucidated and their corresponding activation barriers were estimated. The Co overlayers deposited on the 6-ML Pt(111) substrates inside the (2 × 2) supercell were used. The interdiffusion pathways as elucidated in this perfect heteroepitaxial interface provide insights into the thickness-dependent thermal stability of interfaces qualitatively. The estimates would be an upper bound of the interdiffusion barrier since defects might influence the mechanistic pathways and their barriers. Here, constrained *ab initio* MD and geometry optimizations were carried out. The three bottommost Pt layers were fixed in their optimized positions. One Pt atom at the interface layer was selected, and its z coordinate was increased by 0.3 Å subsequently

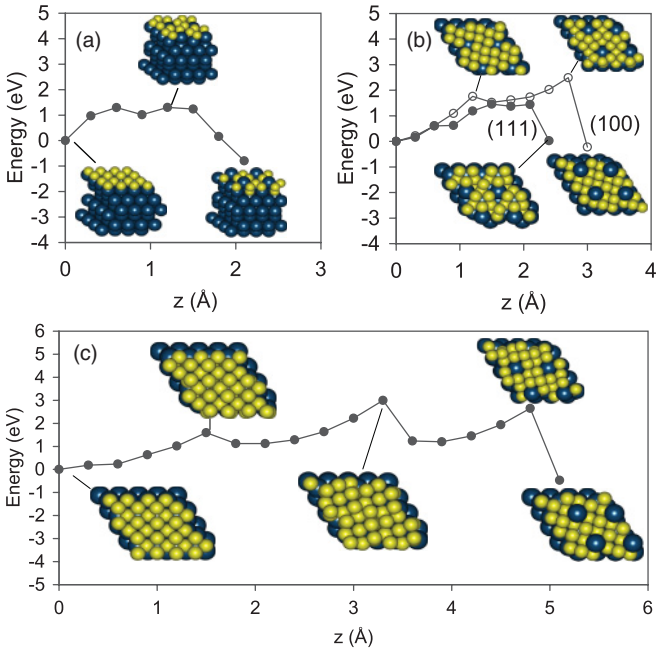

FIG. 5. (Color online) Potential energy profiles of Pt segregation. (a) 1-ML Co(111)/6-ML Pt(111); (b) 2-ML Co(111)/6-ML Pt(111) and 2-ML Co(100)/6-ML Pt(111); (c) 3-ML Co(100)/6-ML Pt(111).

in the constrained MD simulations. In each constrained MD simulation, the system was preheated to 300 K for 750 fs, followed by a 2.8-ps MD simulation at 300 K using a Nosé thermostat.[24] The structure at the end of the trajectory was further optimized, keeping the three bottommost Pt layers and the z coordinate of the selected interfacial Pt atom fixed. The energy profiles of Pt segregation are displayed in Fig. 5, and the estimated segregation barriers are summarized in Table II. As shown in the insets of Fig. 5, the outward motion of the interfacial Pt atom results in a roughening of the upper layers and in a significant change in the atomic connectivity. The surface roughening continued until the space of the vacancy site was sufficiently large to accommodate a cobalt atom. The upper PtCo layers became smoothened while the interfacial vacancy was being filled by the cobalt atom. For the 1–2-ML Co overlayer with (111) orientation, the interdiffusion of Pt and Co was completed when the Pt atoms were raised in the z direction by 2.1–2.4 Å. Therefore, the Pt and Co atoms were exchanged between the two adjacent layers by a "1-2 exchange" mode. The corresponding interdiffusion barriers were estimated to be 1.30 and 1.46 eV for 1- and 2-ML Co overlayers, respectively.

TABLE II. Estimated segregation barrier by the PBE-PAW method.

Cobalt overlayer[a]	Overlayer structure Initial	Final	E_a (eV)[b]	Comment
1 ML	Hexagonal	Hexagonal	1.30	1-2 exchange
2 ML	Hexagonal	Hexagonal	1.46	1-2 exchange
2 ML	Rectangular	Rectangular	2.49	1-3 exchange
3 ML	Rectangular	Rectangular	3.00	1-4 exchange
4 ML	Rectangular	Rectangular	4.20	

[a]Substrate: 6-ML Pt(111).
[b]Segregation barrier.

On the Co overlayers with (100) orientation, the segregation barriers were much larger than those on the Co overlayers with (111) orientation. On the 2-ML Co(100) overlayer, the barrier was estimated to be 2.49 eV. Interestingly, the interfacial vacancy site was not filled until the selected Pt atom reached the outermost layer. Along the segregation path, the interfacial vacancy site and the Co adatom on the outer surface coexisted. Therefore, the interdiffusion process took place in a "1-3 exchange" mode for the 2-ML Co(100) overlayer and a "1-4 exchange" mode for the 3-ML Co(100) overlayer. On the 3-ML Co(100) overlayer, the segregation barrier was even larger (3.00 eV). The selected Pt atom can be "trapped" in the Co overlayers. On the 3-ML Co(100) overlayer, the rate-determining step was due to the interdiffusion of Pt and Co from the first interfacial Co layer to the second interfacial Co layer. On the 4-ML Co(100) overlayer, the segregation barrier was found to be 4.20 eV. Note, however, that the interfacial vacancy site has not yet been filled on the 4-ML Co(100) overlayer model. This may be due to the limited period of simulation time for such a model. Our computed segregation barriers were calculated using an ideally formed Co(100)/Pt(111) without defect. A lower activation barrier was expected if vacancy was introduced.

IV. CONCLUSION

In summary, lattice and electron instability were found to be strongly correlated in the two-dimensional Co/Pt(111) interface. The cobalt monolayer was stable only in the (111) orientation, while the 2-ML cobalt overlayers can exist either in the hexagonal or the rectangular phase. For the thicker cobalt slabs ($\geqslant$3 ML), the cobalt overlayers exist only in the (100) orientation. The reconstruction mechanism can be traced back to the electron instability in **k** space. The surface reconstruction resulted in the retardation of the Pt diffusion at the interface. The computed thickness-dependent segregation tendency was in agreement with the available experimental findings.[6,7] The fundamental understanding will help in the further development of the bimetallic compounds of higher thermal stability. Moreover, this study also contains insights into other systems in which morphology and pattern formation are of interest in two dimensions, e.g., molecular self-assembly on transition-metal surfaces.[25]

ACKNOWLEDGMENTS

We acknowledge Professor John S. Tse for his fruitful discussions, and financial support from Fonds der Chemischen Industrie, Alexander von Humboldt Foundation (W.L.Y.), Hanse Wissenschaftskolleg (W.L.Y.), IHPC Independent Investigatorship (W.L.Y.), and the EWE AG (T.K.). The simulations were performed on the national supercomputer NEC SX-8 at the High Performance Computing Center Stuttgart (HLRS) under Grant No. WLYIM, and on the supercomputing facility allocated at the A*Star Computational Resource Centre (A*CRC).

*yimwl@ihpc.a-star.edu.sg

[1] S. Stavroyiannis, I. Panagiotopoulos, D. Niarchos, J. Christodoulides, Y. Zhang, and G. Hadjipanayis, Appl. Phys. Lett. **73**, 3453 (1998).
[2] V. Stamenkovic, T. Schmidt, P. Ross, and N. Markovic, J. Phys. Chem. B **106**, 11970 (2002).
[3] W. L. Yim and T. Klüner, J. Phys. Chem. C **114**, 7141 (2010).
[4] Y. Gauthier, M. Schmid, S. Padovani, E. Lundgren, V. Bus, G. Kresse, J. Redinger, and P. Varga, Phys. Rev. Lett. **87**, 036103 (2001).
[5] D. Fenske, W.-L. Yim, S. Neuendorf, D. Hoogestraat, D. Greshnykh, H. Borchert, T. Klüner, and K. Al-Shamery, Chem. Phys. Chem. **8**, 654 (2007).
[6] R. Baudoing-Savois, P. Dolle, Y. Gauthier, M. C. Saint-Lager, M. De Santis, and V. Jahns, J. Phys. Condens. Matter **11**, 8355 (1999).
[7] M. C. Saint-Lager, R. Baudoing-Savois, M. De Santis, P. Dolle, and Y. Gauthier, Surf. Sci. **418**, 485 (1998).
[8] A. Cao and G. Veser, Nat. Mater. **9**, 75 (2010).
[9] G. Kresse and J. Furthmüller, Phys. Rev. B **54**, 11169 (1996).
[10] G. Kresse and J. Hafner, Phys. Rev. B **47**, 558 (1993).
[11] G. Kresse and J. Hafner, Phys. Rev. B **49**, 14251 (1994).
[12] S. Baroni, A. D. Corso, S. d. Gironcoli, and P. Giannozzi [http://www.pwscf.org].
[13] S. Baroni, S. de Gironcoli, A. Dal Corso, and P. Giannozzi, Rev. Mod. Phys. **73**, 515 (2001).
[14] A. Atrei, M. Galeotti, U. Bardi, M. Torrini, E. Zanazzi, and G. Rovida, Surf. Rev. Lett. **2**, 279 (1995).
[15] J. P. Perdew, K. Burke, and M. Ernzerhof, Phys. Rev. Lett. **78**, 1396 (1997).
[16] D. Vanderbilt, Phys. Rev. B **41**, 7892 (1990).
[17] G. Kresse and D. Joubert, Phys. Rev. B **59**, 1758 (1999).
[18] N. Marzari, D. Vanderbilt, A. De Vita, and M. C. Payne, Phys. Rev. Lett. **82**, 3296 (1999).
[19] M. Methfessel and A. T. Paxton, Phys. Rev. B **40**, 3616 (1989).
[20] H. J. Monkhorst and J. D. Pack, Phys. Rev. B **13**, 5188 (1976).
[21] Y. Waseda, K. Hirata, and M. Ohtani, High Temp. High Press. **7**, 221 (1975).
[22] F. Vincent and M. Figlarz, C. R. Hebd. Seances Acad. Sci. **264C**, 1270 (1967).
[23] C. Tusche, H. L. Meyerheim, and J. Kirschner, Phys. Rev. Lett. **99**, 026102 (2007).
[24] S. Nosé, J. Chem. Phys. **81**, 511 (1984).
[25] O. Voznyy, J. Dubowski, J. T. Yates Jr., and P. Maksymovych, J. Am. Chem. Soc. **131**, 12989 (2009).